JOURNAL OF COMPUTATIONAL PHYSICS **127,** 2–14 (1996)
ARTICLE NO. 0154

Discretization on Non-Orthogonal, Quadrilateral Grids for Inhomogeneous, Anisotropic Media

I. AAVATSMARK, T. BARKVE, Ø. BØE, AND T. MANNSETH*

Norsk Hydro A/S, Forskningssenteret, N-5020 Bergen, Norway

Received February 24, 1995; revised August 15, 1995

Two classes of discretization methods are proposed for control-volume formulations on quadrilateral grids in two space dimensions. Curvilinear grids are considered as a special case. The methods are applicable for any system of conservation laws where the flux is defined by a gradient law, like Darcy's law for porous-media flow. A strong feature of the methods is the ability to handle media inhomogeneities in combination with full-tensor anisotropy and/or non-orthogonality of the grid. Further properties of the methods will be discussed and examples of their use will be presented. © 1996 Academic Press, Inc.

1. INTRODUCTION

In many flow phenomena, the flux is given by a gradient law $\mathbf{q} = -\mathbf{K}\nabla u$, like Fourier's law of heat conduction, Darcy's law for porous-media flow, or Ohm's law of electric conduction. For a general anisotropic, inhomogeneous medium, the conductivity field $\mathbf{K}$ must be represented by a space-dependent full tensor. Off-diagonal elements in the tensor may exist if the coordinate directions are not aligned with the principal directions for $\mathbf{K}$. Discretization methods for conservation laws are generally not designed to handle both inhomogeneity and general anisotropy. The purpose of this study is development of methods to improve this situation for non-orthogonal quadrilateral grids in two space dimensions.

Large discontinuities in medium properties require construction of numerical schemes with a proper definition of the effective conductivity across cell interfaces. The methods presented in this paper will produce a generalization of the harmonic average commonly applied for a diagonal tensor $\mathbf{K}$ and orthogonal grids [3].

To satisfy local continuity in flux between grid cells with strong discontinuities in conductivity, control-volume methods are especially well suited. For time-dependent problems with large solution gradients, it is important that the methods can be combined with a fully implicit time stepping. The study of such methods for inhomogeneous, anisotropic problems have been the subject of several recent contributions [1, 5, 7–9]. In Ref. [1], continuity conditions at cell interfaces are used to construct two discretization methods for non-orthogonal curvilinear grids. One of these discretizations is a special case of a larger class of methods published independently in Refs. [7, 8]. A similar method for elliptic equations presented in Ref. [5] will lead to time-dependent effective conductivities in the vicinity of a time-dependent source, and an extension to parabolic equations does not exist.

Alternative approaches for quadrilateral grids are the application of traditional Galerkin methods [10] and control-volume finite-element methods (CVFE) [12, 13]. For elements with internal discontinuities in conductivity, Galerkin methods produce an effective conductivity that resembles an arithmetic, rather than a harmonic, mean and do not yield continuous fluxes. Nodes can be located at the discontinuities, but this may be unfortunate for problems with a solution discontinuity coinciding with a jump in conductivity, typical for multi-phase porous-media flow. For CVFE-methods, no proper technique for handling discontinuities at control-volume boundaries exists. Mixed finite-element methods [4] do not suffer from these shortcomings and can be applied to inhomogeneous, anisotropic problems [6]. However, these methods are restricted to a sequential solution for a system of non-linear conservation laws.

Non-orthogonal grids, as well as anisotropy, will generally require a flux discretization molecule involving more than two grid points, with a corresponding cell molecule with more than five grid points. Several finite-difference methods with a nine-point cell molecule are described in the literature, but these methods are commonly designed to reduce grid-orientation effects on a regular grid in a homogeneous medium [15]. Methods discussed in this presentation will all reduce to the standard five-point stencil for this situation.

The aim of this paper is to give a more detailed presentation of the discretization methods outlined in Ref. [1]. Non-orthogonal curvilinear grids will now be investigated as a special case of irregular quadrilaterals. Although having

* Now with RF-Rogalandsforskning, Thormøhlensgt. 55, N-5008 Bergen, Norway.

0021-9991/96 $18.00

wider applicability, the methods will be introduced based on model equations for multi-phase flow in porous media. Important effects of rock anisotropy and inhomogeneities, along with complex model geometry, motivate the use of the presented methods in reservoir simulation. Inactive grid cells and internal no-flow cell faces, commonly featured in reservoir simulation, will be handled by the methods with almost no increase in complexity.

An introduction to the basic control-volume formulation is given in Section 2. The discretization methods are presented in Section 3, while Section 4 discusses properties of the methods. The latter section also demonstrates use of the methods.

2. CONTROL-VOLUME FORMULATION

Strong non-linearities in model equations often necessitates use of a fully implicit time-discretization. A fully implicit control-volume formulation for a general system of conservation laws can be expressed as

$$m_\alpha^n - m_\alpha^{n-1} + \Delta t^n \sum_j f_{\alpha j}^n = q_\alpha^n, \tag{2.1}$$

where Δt is the time step and the superscript n denotes the time level. For multi-phase porous-media flow, m_α is the accumulated mass of phase α, and $f_{\alpha j}$ is the phase flux through surface number j in the control volume. The source term q_α represents production or injection wells in the reservoir. The flux is given by Darcy's law as

$$f_{\alpha j}^n = -\int_{S_j} (\lambda_\alpha \mathbf{K} \nabla u_\alpha)^n \cdot \mathbf{n}\, dS. \tag{2.2}$$

The relative mobility of phase α is denoted λ_α. The permeability tensor $\mathbf{K}$ is allowed to contain off-diagonal terms, but will be assumed to be symmetric, positive definite. u_α is the phase potential, and $\mathbf{n}$ is the unit normal vector to the cell interface. To simplify the presentation, phase transfers have been neglected in (2.2).

Assuming that the relative mobility has a constant value $\lambda_{\alpha j}^n$ along the cell interface, the flux can be expressed as

$$\begin{aligned} f_{\alpha j}^n &= -\lambda_{\alpha j}^n \int_{S_j} \nabla u_\alpha^n \cdot \mathbf{w}\, dS, \\ \mathbf{w} &= \mathbf{K}\mathbf{n}. \end{aligned} \tag{2.3}$$

For a curvilinear grid, a similar flux expression is found if a transformation to the usual computational space is performed: In two space dimensions, a curvilinear grid can be described by a coordinate transformation from the physical Cartesian space (x, y) into a computational space (ξ, η), where the grid is orthogonal and equidistant. The coordinate mapping should be one-to-one, continuously differentiable, and boundary preserving. In the computational space, the flux can be expressed as

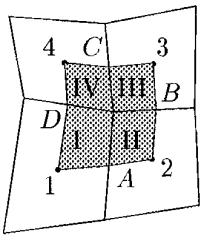

FIG. 1. Grid cells with interaction region.

$$\begin{aligned} f_{\alpha j}^n &= -\lambda_{\alpha j}^n \int_{S_j^*} \nabla^* u_\alpha^n \cdot \mathbf{w}^*\, dS^*, \\ \mathbf{w}^* &= |J|\, (\nabla\xi \mathbf{K} \nabla\chi, \nabla\eta \mathbf{K} \nabla\chi). \end{aligned} \tag{2.4}$$

Here, ∇^* is the gradient operator in the coordinates (ξ, η), and J is the Jacobian determinant for the coordinate transformation. If the cell interface number j in the curvilinear space is a level curve for ξ, then $\chi = \xi$, while $\chi = \eta$ if the interface is a level curve for η.

3. FLUX-CONSERVATIVE DISCRETIZATION METHODS

This section will consider discrete approximations of the flux term in the control-volume formulation. Discretization in the physical space based on (2.3) will be presented first, but as the flux expressions in (2.3) and (2.4) have an identical form, the methods are directly applicable also in the computational space for a curvilinear grid. Due to the regularity of the grid in the computational space, implementation of the methods simplify considerably for curvilinear grids.

For all methods, the relative mobility $\lambda_{\alpha j}^n$ will be evaluated by upstream weighting based on the sign of $(-\nabla u_\alpha^n \cdot \mathbf{w})$, and for presentational purposes only, the value $\lambda_{\alpha j}^n = 1$ will be assumed in the remaining part of the paper. Also, the phase subscript α and the time superscript n will be dropped.

3.1. *Interaction Region*

Consider four adjacent grid cells in a two-dimensional region, as shown in Fig. 1. The coordinates of a general point P will be denoted (x_P, y_P) and the corresponding value of the unknown u_P. The cell centers are enumerated 1, 2, 3, and 4, and the mid points of the cell interfaces are named A, B, C, and D, respectively. These eight points span a polygon which will be called the *interaction region* of the four cells.

The flux across the part of a cell interface lying inside

of the interaction region will be defined by a linear combination of the four grid-cell values u_i in the region: If E is the common corner point of the four grid cells, the flux f_A across the interface segment AE can be expressed as

$$f_A = \sum_{i=1}^{4} t_{Ai} u_i. \tag{3.1}$$

The coefficients t_{Ai} will be called the *transmissibilities* associated with AE. Since the flux must be zero when $\{u_i\}$ is a constant vector, it follows that $\sum_{i=1}^{4} t_{Ai} = 0$. The domain of the differential equations is covered by non-overlapping interaction regions, and the transmissibilities for a given cell interface are calculated by assembling contributions from the two interaction regions involved. This leads to a six-point flux-molecule (nine-point cell molecule). For special cases where the grid is orthogonal and the grid axes are aligned with the principal directions of $\mathbf{K}$, a two-point flux molecule (five-point cell molecule) is retained.

For an interface adjacent to an outer boundary, an interaction region is defined by extending the domain of the differential equation with extra grid cells. A homogeneous Neumann condition is, for instance, modeled by defining the extra grid cells as inactive. Handling of inactive grid cells will be further discussed in Section 4.3.

Alternatively, the interaction region can be defined as a rectangle with boundaries equal to straight lines between the grid points 1, 2, 3, and 4. This definition could lead to interaction regions including volume *not* part of the four grid cells, if the grid is very irregular. For a curvilinear grid, however, this alternative definition coincides with the definition above, when the discretization is performed in the computational space.

The interaction region consists of four distinct sub-regions, denoted by Roman numerals in Fig. 1. When calculating transmissibilities for a given interface, say AE, a linear variation in the solution variable will be assumed for each sub-region:

$$\begin{aligned} u^{(\mathrm{I})} &= u_1 + E_1 X^{(\mathrm{I})} + F_1 Y^{(\mathrm{I})}, \\ u^{(\mathrm{II})} &= u_2 + E_2 X^{(\mathrm{II})} + F_2 Y^{(\mathrm{II})}, \\ u^{(\mathrm{III})} &= u_3 + E_3 X^{(\mathrm{III})} + F_3 X^{(\mathrm{III})}, \\ u^{(\mathrm{IV})} &= u_4 + E_4 X^{(\mathrm{IV})} + F_4 Y^{(\mathrm{IV})}. \end{aligned} \tag{3.2}$$

$X^{(\mathrm{i})}$ and $Y^{(\mathrm{i})}$ are local coordinates for sub-region (i), defined with origin in the grid point i and axes along the interaction region boundary. That is, for sub-region I:

$$\begin{aligned} x &= x_1 + (x_A - x_1) X^{(\mathrm{I})} + (x_D - x_1) Y^{(\mathrm{I})}, \\ y &= y_1 + (y_A - y_1) X^{(\mathrm{I})} + (y_D - y_1) Y^{(\mathrm{I})}. \end{aligned} \tag{3.3}$$

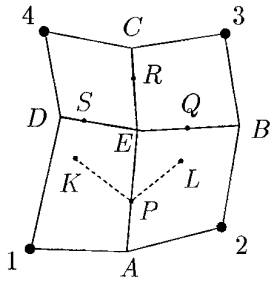

FIG. 2. Interaction region.

The coefficients E_i and F_i will be determined as linear functions of the grid point unknowns u_i by imposing continuity constraints at cell interfaces. Flux continuity across each of the four interfaces will lead to four equations. Eight additional equations are defined by requiring continuity in the solution variable, as continuity in two points at the interface will guarantee full continuity along the interface when the solution approximation is piecewise linear. In total, 12 equations for the eight unknown coefficients E_i and F_i are obtained, i.e., an overdetermined system. Sections 3.2 and 3.3 will discuss two alternative ways of imposing a reduced number of continuity constraints at the interfaces.

The overdetermined system reflects that for two space dimensions, a piecewise linear solution of the equation $\nabla \cdot (\mathbf{K}\nabla u) = 0$ does not exist for a piecewise inhomogeneous medium. For a single space dimension, an exact piecewise linear solution does exist. Application of larger solution spaces than the piecewise linear space may overcome the problem and will be investigated in future research.

Associated to the interface AE, two vectors $\mathbf{w}_A^{(\mathrm{I})}$ and $\mathbf{w}_A^{(\mathrm{II})}$ can be defined, based on values for the permeability tensor in the two sub-regions. In the following, these two vectors will be defined with equal orientation, associated with the edge. Recalling the definition, $\mathbf{w} = \mathbf{Kn}$, the vector $\mathbf{n}_A$ will be oriented from grid cell 1 towards grid cell 2, and the flux will be defined positive in that direction. From the positive definiteness of $\mathbf{K}$, the vector $\mathbf{w}_A$ then also points towards grid cell 2. Definitions for the other edges follow by rotation.

Let P be a point located arbitrarily on the line segment AE. Also, let K and L be two points located arbitrarily along straight lines through P with direction $\mathbf{w}_A^{(\mathrm{I})}$ and $\mathbf{w}_A^{(\mathrm{II})}$, respectively, as shown in Fig. 2. Based on the linear variation in u, the flux through interface AE *out* of sub-region I is given by

$$f_A^{(\mathrm{I})} = S_A w_A^{(\mathrm{I})} \frac{u_K^{(\mathrm{I})} - u_P^{(\mathrm{I})}}{l_{KP}}. \tag{3.4}$$

Here, S_A is the area of the interface AE, and w is the 2-

norm of the vector **w**. Also, l_{KP} is the length of the line segment KP. Similarly, the flux through AE *into* sub-region II is given by

$$f_A^{(\mathrm{II})} = S_A w_A^{(\mathrm{II})} \frac{u_P^{(\mathrm{II})} - u_L^{(\mathrm{II})}}{l_{PL}}. \tag{3.5}$$

Now assume that the solution is continuous at the point P. Conservation implies that the two fluxes are identical, and this can be used to eliminate the value of u in P:

$$f_A^{(\mathrm{I})} = f_A^{(\mathrm{II})} = f_A = S_A \overline{w}_A \frac{u_K^{(\mathrm{I})} - u_L^{(\mathrm{II})}}{l_{KP} + l_{PL}}. \tag{3.6}$$

$\overline{w}_A$ is a harmonic average, defined by

$$\frac{l_{KP} + l_{PL}}{\overline{w}_A} = \frac{l_{KP}}{w_A^{(\mathrm{I})}} + \frac{l_{PL}}{w_A^{(\mathrm{II})}}. \tag{3.7}$$

For an orthogonal grid and a diagonal permeability tensor, this expression reduces to the harmonic average commonly applied in reservoir simulators. Equations (3.4)–(3.7) have been obtained by Ref. [9], apart from an apparent misprint in the presented definition of $\overline{w}_A$.

Defining $u_L^{(\mathrm{II})}$ and $u_K^{(\mathrm{I})}$ by using (3.2), the flux f_A will be expressed as a linear function of the four grid unknowns u_i. The coefficients in this expression will define the transmissibilities introduced in (3.1). For a complete description, continuity constraints must be selected, alternatively as described in the two next sections.

3.2. *O-Methods*

With a linear potential approximation, it is not possible to impose continuity in both flux and potential at all points of the interfaces inside of the interaction region. This section presents a first alternative for a reduced system of constraints for the eight unknowns E_i and F_i in (3.2), as basis for the transmissibility calculation.

For grid cell I, the flux out of the cell through interface AE can be expressed by substituting (3.2) into (2.3):

$$f_A^{(\mathrm{I})} = -S_A \left[E_1 \nabla X^{(\mathrm{I})} + F_1 \nabla Y^{(\mathrm{I})}\right] \cdot \mathbf{w}_A^{(\mathrm{I})}. \tag{3.8}$$

Expressions for the other grid cells and the other interfaces are similar. Hence, flux continuity through all four interfaces requires that

$$\begin{aligned}
&[\mathrm{E}_1 \nabla X^{(\mathrm{I})} + F_1 \nabla Y^{(\mathrm{I})}]_A \cdot \mathbf{w}_A^{(\mathrm{I})} \\
&\quad = [E_2 \nabla X^{(\mathrm{II})} + F_2 \nabla Y^{(\mathrm{II})}]_A \cdot \mathbf{w}_A^{(\mathrm{II})}, \\
&[E_2 \nabla X^{(\mathrm{II})} + F_2 \nabla Y^{(\mathrm{II})}]_B \cdot \mathbf{w}_B^{(\mathrm{II})} \\
&\quad = [E_3 \nabla X^{(\mathrm{III})} + F_3 \nabla Y^{(\mathrm{III})}]_B \cdot \mathbf{w}_B^{(\mathrm{III})}.
\end{aligned} \tag{3.9}$$

FIG. 3. Point couplings in O-methods and U-methods.

$$\begin{aligned}
&[E_3 \nabla X^{(\mathrm{III})} + F_3 \nabla Y^{(\mathrm{III})}]_C \cdot \mathbf{w}_C^{(\mathrm{III})} \\
&\quad = [E_4 \nabla X^{(\mathrm{IV})} + F_4 \nabla Y^{(\mathrm{IV})}]_C \cdot \mathbf{w}_C^{(\mathrm{IV})}, \\
&[E_4 \nabla X^{(\mathrm{IV})} + F_4 \nabla Y^{(\mathrm{IV})}]_D \cdot \mathbf{w}_D^{(\mathrm{IV})} \\
&\quad = [E_1 \nabla X^{(\mathrm{I})} + F_1 \nabla Y^{(\mathrm{I})}]_D \cdot \mathbf{w}_D^{(\mathrm{I})},
\end{aligned}$$

In addition, four continuity conditions for the potential u will be used. The point P was defined arbitrarily along the interface AE, and similarly, the points Q, R, and S are defined arbitrarily along each of the other three interfaces, as shown in Fig. 2. Potential continuity at these four points leads to the equations

$$\begin{aligned}
u_1 + E_1 X_P^{(\mathrm{I})} + F_1 Y_P^{(\mathrm{I})} &= u_2 + E_2 X_P^{(\mathrm{II})} + F_2 Y_P^{(\mathrm{II})}, \\
u_2 + E_2 X_Q^{(\mathrm{II})} + F_2 Y_Q^{(\mathrm{II})} &= u_3 + E_3 X_Q^{(\mathrm{III})} + F_3 Y_Q^{(\mathrm{III})}, \\
u_3 + E_3 X_R^{(\mathrm{III})} + F_3 Y_R^{(\mathrm{III})} &= u_4 + E_4 X_R^{(\mathrm{IV})} + F_4 Y_S^{(\mathrm{IV})}, \\
u_4 + E_4 X_S^{(\mathrm{IV})} + F_4 Y_S^{(\mathrm{IV})} &= u_1 + E_1 X_S^{(\mathrm{I})} + F_1 Y_S^{(\mathrm{I})}.
\end{aligned} \tag{3.10}$$

The eight equations define E_i and F_i as linear functions of the four grid cell values u_i. Let the expressions for E_1 and F_1 be stated as

$$E_1 = \sum_{i=1}^{4} E_{1i} u_i, \quad F_1 = \sum_{i=1}^{4} F_{1i} u_i. \tag{3.11}$$

As the flux is continuous across the interface AE, f_A is given by (3.8). Combining this equation with (3.11), it follows that

$$f_A = \sum_{i=1}^{4} \left\{-S_A \left[E_{1i} \nabla X^{(\mathrm{I})} + F_{1i} \nabla Y^{(\mathrm{I})}\right] \cdot \mathbf{w}_A^{(\mathrm{I})}\right\} u_i. \tag{3.12}$$

Comparison with (3.1) shows that the expression in the braces is the transmissibility t_{Ai}.

Depending on the precise definition of the continuity points, P, Q, R, and S, a class of methods is constructed. A natural choice would be to let these points coincide with the points A, B, C, and D. Alternatively, P can be defined as the midpoint between A and E etc. In Fig. 3, straight

lines are drawn between pairs of grid points linked by a continuity condition at their common cell interface. The class of methods described above will be termed *O-methods* after the stylized "O" formed by such lines in the left part of Fig. 3. O-methods were introduced by the authors [1], and independently by Refs. [7, 8].

3.3. *U-Methods*

To achieve full flux and potential continuity at an edge, a single flux condition and two potential conditions are required, when the potential is linear. O-methods are based on a single flux condition and a single potential condition at each of the four edges in an interaction region. An alternative way of reducing the continuity requirements will now be presented: For calculation of the transmissibilities associated with interface AE, the following flux conditions are imposed:

$$\begin{aligned}
&[E_1\nabla X^{(\mathrm{I})} + F_1\nabla Y^{(\mathrm{I})}]_A \cdot \mathbf{w}_A^{(\mathrm{I})} \\
&\quad = [E_2\nabla X^{(\mathrm{II})} + F_2\nabla Y^{(\mathrm{II})}]_A \cdot \mathbf{w}_A^{(\mathrm{II})}, \\
&[E_2\nabla X^{(\mathrm{II})} + F_2\nabla Y^{(\mathrm{II})}]_B \cdot \mathbf{w}_B^{(\mathrm{II})} \\
&\quad = [E_3\nabla X^{(\mathrm{III})} + F_3\nabla Y^{(\mathrm{III})}]_B \cdot \mathbf{w}_B^{(\mathrm{III})}, \\
&[E_4\nabla X^{(\mathrm{IV})} + F_4\nabla Y^{(\mathrm{IV})}]_D \cdot \mathbf{w}_d^{(\mathrm{IV})} \\
&\quad = [E_1\nabla X^{(\mathrm{I})} + F_1\nabla Y^{(\mathrm{I})}]_D \cdot \mathbf{w}_D^{(\mathrm{I})}.
\end{aligned} \tag{3.13}$$

The interface for which the transmissibilities are calculated will be termed the *central edge*, and the two other interfaces at which flux conditions are imposed will be denoted *non-central edges*. No condition at all will be required at the interface opposite to the central edge, and this interface will be called the *unconstrained edge.* The point couplings shown in the right part of Fig. 3 form a stylized letter "U," motivating the name *U-methods* for this technique.

Potential continuity will be required at the points P, Q, and S, as for O-methods. The two degrees of freedom associated with edge CE in O-methods, are now applied to impose continuity of the potential at point E at both the non-central edges:

$$\begin{aligned}
u_1 + E_1X_P^{(\mathrm{I})} + F_1Y_P^{(\mathrm{I})} &= u_2 + E_2X_P^{(\mathrm{II})} + F_2Y_P^{(\mathrm{II})}, \\
u_2 + E_2X_Q^{(\mathrm{II})} + F_2Y_Q^{(\mathrm{II})} &= u_3 + E_3X_Q^{(\mathrm{III})} + F_3Y_Q^{(\mathrm{III})}, \\
u_2 + E_2X_E^{(\mathrm{II})} + F_2Y_E^{(\mathrm{II})} &= u_3 + E_3X_E^{(\mathrm{III})} + F_3Y_E^{(\mathrm{III})}, \\
u_4 + E_4X_S^{(\mathrm{IV})} + F_4Y_S^{(\mathrm{IV})} &= u_1 + E_1X_S^{(\mathrm{I})} + F_1Y_S^{(\mathrm{I})}, \\
u_4 + E_4X_E^{(\mathrm{IV})} + F_4Y_E^{(\mathrm{IV})} &= u_1 + E_1X_E^{(\mathrm{I})} + F_1Y_E^{(\mathrm{I})}.
\end{aligned} \tag{3.14}$$

This ensures full potential continuity at these edges. The eight equations in (3.13) and (3.14) define the unknowns E_i and F_i as linear functions of u_i, leading to the transmissibilities in the same manner as for O-methods. U-methods were introduced simultaneously with O-methods by the authors [1].

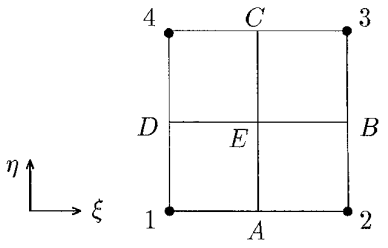

FIG. 4. Interaction region in computational space.

3.4. *O- and U-Method for Curvilinear Grids*

The computational grid in the curvilinear space is orthogonal and equidistant, and the transmissibility calculations may simplify significantly. Let the segments AE and BE in the computational space both have length unity; confer Fig. 4. In (2.4), S_j^* is then also unity, and fluxes in the ξ- and η-directions are given by

$$\begin{aligned}
f_\xi &= a\frac{\partial u}{\partial \xi} + c\frac{\partial u}{\partial \eta}, \\
f_\eta &= c\frac{\partial u}{\partial \xi} + b\frac{\partial u}{\partial \eta},
\end{aligned} \tag{3.15}$$

respectively. The coefficients a, b, and c correspond to components in the vector $\mathbf{w}^*$; confer (2.4):

$$\begin{aligned}
a &= -|J|\nabla\xi\mathbf{K}\nabla\xi, \\
b &= -|J|\nabla\eta\mathbf{K}\nabla\eta, \\
c &= -|J|\nabla\xi\mathbf{K}\nabla\eta.
\end{aligned} \tag{3.16}$$

In the remaining part of this paper, the point P will be chosen to coincide with the point A, and similarly for the three other points Q, R, and S. The methods constructed in this manner will be termed *the* O-method and *the* U-method, respectively.

For the O-method, the linearity assumption for u, stated in (3.2), and the flux continuity conditions, (3.9), can then be simplified to the following form:

$$\begin{aligned}
&a^{(\mathrm{I})}(u_A - u_1) + c^{(\mathrm{I})}(u_D - u_1) \\
&\quad = a^{(\mathrm{II})}(u_2 - u_A) + c^{(\mathrm{II})}(u_B - u_2) = \sum t_{Ai}u_i, \\
&c^{(\mathrm{II})}(u_2 - u_A) + b^{(\mathrm{II})}(u_B - u_2) \\
&\quad = c^{(\mathrm{III})}(u_3 - u_C) + b^{(\mathrm{III})}(u_3 - u_B) = \sum t_{Bi}u_i, \\
&a^{(\mathrm{IV})}(u_C - u_4) + c^{(\mathrm{IV})}(u_4 - u_D)
\end{aligned} \tag{3.17}$$

$$= a^{(\mathrm{III})}(u_3 - u_C) + c^{(\mathrm{III})}(u_3 - u_B) = \sum t_{Ci}u_i,$$

$$c^{(\mathrm{IV})}(u_C - u_4) + b^{(\mathrm{IV})}(u_4 - u_D)$$
$$= c^{(\mathrm{I})}(u_A - u_1) + b^{(\mathrm{I})}(u_D - u_1) = \sum t_{Di}u_i.$$

The potential continuity constraints have been used directly in these equations. To write the system in matrix form, define the two column matrices

$$\mathbf{u} = [u_1, u_2, u_3, u_4]^{\mathrm{T}}, \quad \mathbf{u}_e = [u_A, u_B, u_C, u_D]^{\mathrm{T}}. \tag{3.18}$$

The matrix form of (3.17) is then

$$\mathbf{A}\mathbf{u}_e + \mathbf{B}\mathbf{u} = \mathbf{C}\mathbf{u}_e + \mathbf{D}\mathbf{u} = \mathbf{T}\mathbf{u}, \tag{3.19}$$

where **A**, **B**, **C**, and **D** are 4×4 matrices with elements a, b, and c; and **T** is a matrix where the elements in each row are the transmissibilities for an interface segment. Equation (3.19) is easily solved for the transmissibilities, by eliminating the edge values $\mathbf{u}_e$:

$$\mathbf{T} = \mathbf{A}(\mathbf{A} - \mathbf{C})^{-1}(\mathbf{D} - \mathbf{B}) + \mathbf{B}. \tag{3.20}$$

For the O-method, the continuity constraints at the interfaces are independent of the location of the central edge, and all transmissibilities for the interaction region are given by a single expression, as (3.20). This is not the case for the U-method, where the flux conditions depend on the location of the central edge: For this method, transmissibilities are calculated for each interface separately. For AE as the central edge, the two potential continuity conditions at the point E can be stated as

$$\begin{aligned} u_E^{(\mathrm{I})} &= u_A + u_D - u_1 = u_D + u_C^{(\mathrm{IV})} - u_4 = u_E^{(\mathrm{IV})}, \\ u_E^{(\mathrm{II})} &= u_A + u_B - u_2 = u_B + u_C^{(\mathrm{III})} - u_3 = u_E^{(\mathrm{III})}. \end{aligned} \tag{3.21}$$

These equations can be used to eliminate the values $u_C^{(*)}$ in the two flux conditions at the non-central edges. The whole set of flux conditions then reads

$$\begin{aligned} &a^{(\mathrm{I})}(u_A - u_1) + c^{(\mathrm{I})}(u_D - u_1) \\ &\quad = a^{(\mathrm{II})}(u_2 - u_A) + c^{(\mathrm{II})}(u_B - u_2) = \sum t_{Ai}u_i, \\ &c^{(\mathrm{II})}(u_2 - u_A) + b^{(\mathrm{II})}(u_B - u_2) \\ &\quad = c^{(\mathrm{III})}(u_2 - u_A) + b^{(\mathrm{III})}(u_3 - u_B), \\ &c^{(\mathrm{IV})}(u_A - u_1) + b^{(\mathrm{IV})}(u_4 - u_D) \\ &\quad = c^{(\mathrm{I})}(u_A - u_1) + b^{(\mathrm{I})}(u_D - u_1). \end{aligned} \tag{3.2}$$

The U-method transmissibilities for the edge AE are now given as the first row in a matrix of the form given in (3.20), with definitions of the matrices **A**, **B**, **C**, and **D** now inferred from (3.22).

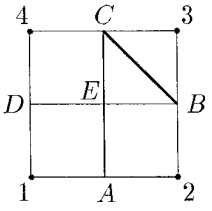

FIG. 5. O-method. Interaction region with axis of rotation, BC.

3.5. *Mechanistic Interpretation of O- and U-Methods*

For a better understanding of similarities and differences between O- and U-methods, a mechanistic interpretation of the methods will be given. This mechanistic view will also be helpful when analyzing special flow situations in Section 4.5. For simplicity, the discussion will be based on the O- and the U-methods for curvilinear grids defined in the previous section.

In the calculation of transmissibilities for a given edge, a piecewise linear variation in the potential is assumed inside of the interaction region. This linear variation can be regarded as four potential planes defined inside the region. The angle between two adjacent planes can be measured as the angle between lines defined by the vectors $\mathbf{w}^*$ in the respective grid cells, and the flux continuity condition applied in the calculations can be interpreted as a condition on this angle. For a homogeneous interaction region, all angles are zero.

A potential-continuity condition applied at an interface point can be viewed as a hinge where two planes are linked together. For all flow situations, the potential planes must obey these mechanistic constraints. The O- and the U-methods are using alternative continuity conditions, resulting in different mechanistic behavior of the potential planes.

In the O-method, the couplings within an interaction region are independent of the location of the central edge. Consider the interaction region shown in Fig. 5, and let $u_1 = u_2 = u_3 = u_4$, initially. If now u_3 is increased, the O-method will result in tilting of the plane III as shown in Fig. 6. Since hinges exist at points B and C, the only feasible

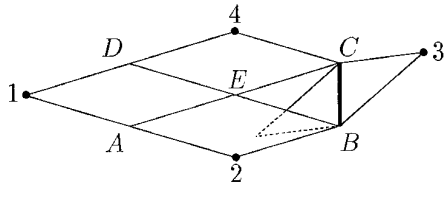

FIG. 6. O-method. Rotated plane in interaction region.

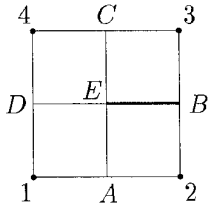

FIG. 7. U-method. Coupling at a non-central edge. Interaction region with axis of rotation, BE.

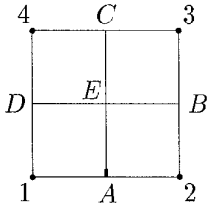

FIG. 9. U-method. Coupling at the central edge. Interaction region with point of rotation, A.

movement of plane III relative to these points in the planes II and IV, is a rotation with respect to the axis, BC. The tilting of plane III will cause the other planes to move as well, to satisfy the continuity conditions. These movements are not shown in Fig. 6. All movements will be composed of translations of the hinges at A, B, C, and D, in combination with rotations with respect to axes through these points.

In the U-method, the couplings within an interaction region depend on the location of the central edge. There is a single hinge on the central edge, AE, while the non-central edges, BE and DE, have two hinges each. Plane III and plane IV are then completely linked to plane II and plane I, respectively, along their common edges. Again, let $u_1 = u_2 = u_3 = u_4$, initially, and let u_3 be increased. The only feasible movement of plane III relative to points B and E in plane II, is a rotation with respect to the axis, BE, as shown in Fig. 7 and Fig. 8. If the tensor $\mathbf{K}$ has equal values in Cells 2 and 3, the angle between the $\mathbf{w}^*$-vectors in planes II and III is zero. As the two planes are completely linked along BE, they will then behave as a single plane.

For the U-method, a different situation arises if u_2 is increased when $u_1 = u_2 = u_3 = u_4$ initially. Feasible movements of plane II relative to point A in plane I are rotations with respect to an axis through A, as shown in Fig. 9 and Fig. 10. The mechanistic description presented in this section will be further used in Section 4.5 to analyze special flow situations.

3.6. *Multi-phase Flow*

In this paper, the O- and U-methods are presented within the framework of single-phase flow. An additional difficulty arises when applying any method with a six-point flux molecule to multi-phase flow: Discretization at edges in the grid adjacent to fluid contacts. This problem is discussed in the context of porous-media flow in Ref. [1], where some solutions are presented.

4. PROPERTIES OF THE METHODS

Both the O- and the U-method are designed to handle media inhomogeneities, in combination with full-tensor anisotropy and/or non-orthogonality of the grid. As shown in Section 3.1, this is accomplished by generalizing the principle of harmonic averaging, commonly applied with a two-point flux molecule. Although based on the same idea, some theoretical and numerical properties of the two methods will be different, as discussed in the following section.

4.1. *Symmetry*

As $\mathbf{K}$ is assumed to be symmetric, appropriate boundary conditions also lead to a symmetric operator $\nabla \cdot (\mathbf{K}\nabla)$. By simple counterexamples, it is easily shown that discretization by the U-method in general does not lead to a symmetric matrix. For the O-method, no such counterexample has been found, but a general symmetry property of this method is still not proved. In Ref. [8], the O-method is shown to lead to a symmetric matrix if the grid is orthogonal and the medium is anisotropic and homogeneous.

4.2. *Convergence Properties*

A general convergence analysis of the O- and U-methods is difficult to carry through, due to the local character of the

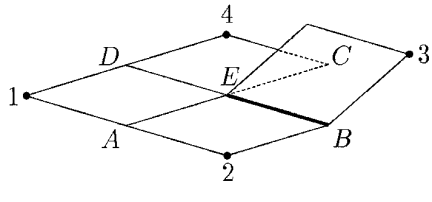

FIG. 8. U-method. Coupling at a non-central edge. Rotated plane in interaction region.

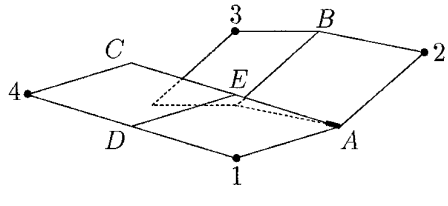

FIG. 10. U-method. Coupling at the central edge. Rotated planes in interaction region.

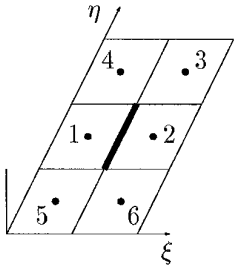

FIG. 11. Part of uniform, non-orthogonal grid. Flux molecule for ξ-level-curve edge.

transmissibility calculations and the subsequent assembly procedure. Convergence properties for some inhomogeneous test examples will be studied in Section 4.4. In the following, consider the simplified case where the coefficients a, b, and c defined in (3.16) are constants. An example problem satisfying the above condition is the uniform, non-orthogonal grid shown in Fig. 11, defined for a homogeneous medium with a constant anisotropy.

Let f_ξ denote the flux at an edge in the grid which is a level curve for ξ. Analogously, f_η is the flux through an interface which is a level curve for η. Analytical expression for these fluxes are given in (3.15). The cell numeration in Fig. 11 will be used to define the numerical flux approximation for f_ξ, while the numeration in Fig. 12 is applied for f_η. For the O-method, straightforward treatment of the continuity conditions leads to

$$\begin{aligned} f_\xi &= \left(a - \frac{c^2}{2b}\right)(u_2 - u_1) + \frac{c}{4}\left(1 + \frac{c}{b}\right)(u_3 - u_5) \\ &\quad + \frac{c}{4}\left(1 - \frac{c}{b}\right)(u_4 - u_6), \\ f_\eta &= \left(b - \frac{c^2}{2a}\right)(u_2 - u_1) + \frac{c}{4}\left(1 - \frac{c}{a}\right)(u_5 - u_3) \\ &\quad + \frac{c}{4}\left(1 + \frac{c}{a}\right)(u_6 - u_4). \end{aligned} \tag{4.1}$$

For the U-method, the expressions read

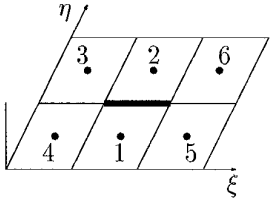

FIG. 12. Part of uniform, non-orthogonal grid. Flux molecule for η-level-curve edge.

$$\begin{aligned} f_\xi &= a(u_2 - u_1) + \tfrac{1}{4}c\{(u_3 - u_6) + (u_4 - u_5)\}, \\ f_\eta &= b(u_2 - u_1) + \tfrac{1}{4}c\{(u_6 - u_3) + (u_5 - u_4)\}. \end{aligned} \tag{4.2}$$

If c equals zero, both methods reduce to identical two-point flux formulas, but in the general case, the methods may lead to significantly different transmissibilities. Note that the U-method weights the points 3, 4, 5, and 6 equally, as opposed to the uneven weighting in the O-method.

Equations (3.15), (3.16), and (4.2) show that the U-method constructs an approximation of $\nabla^* u$ which is independent of the coefficients a, b, and c. The O-method applies a gradient approximation where the weighting of the involved grid cells depends on these coefficients. An immediate consequence is seen for the directional derivative in the expression $(-\mathbf{w}^* \cdot \nabla^* u)$: The O-method gradient depends on $\mathbf{w}^*$ while the U-method gradient does not.

By assembling all fluxes for a grid cell and performing Taylor-expansions of the potentials in the involved neighboring grid cells, we find that both methods are second-order accurate when a, b, and c are constants. For the U-method, an assembling of fluxes given by (4.2) leads to the traditional curvilinear discretization found, e.g., in Ref. [14]. This method was suggested for problems in isotropic and homogeneous media (air).

The convergence results presented here were briefly stated by the authors in Ref. [1]. The case of general constant coefficients a, b, and c also covers an orthogonal grid defined for an anisotropic, homogeneous medium, for which second-order convergence of the O-method was proven in Ref. [8].

4.3. *Handling of Inactive Cells and Interfaces*

An edge in the grid with a zero-flux condition, is called *inactive.* Inactive edges occur in connection with no-flow outer boundaries and in connection with impermeable zones within the model. Thin impermeable zones are modeled by inactive edges in active grid cells, while thicker zones are modeled by inactive grid cells, i.e., grid cells where all edges are inactive. Clearly, a correct treatment of inactive edges is necessary to model fluid flow correctly.

With a two-point flux molecule, the treatment of inactive edges is straightforward: There is no need to calculate the flux at the inactive edge, and none of the flux calculations

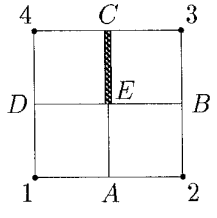

FIG. 13. Interaction region with inactive unconstrained edge.

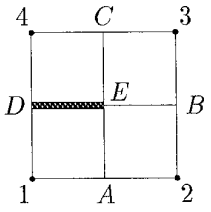

FIG. 14. Interaction region with inactive non-central edge.

at the other edges in the grid are influenced by the inactive edge. With a six-point flux molecule, an inactive edge will influence flux calculations at adjacent edges in the grid. For O- and U-methods, inactive edges inside an interaction region are handled by replacing the corresponding continuity conditions by zero-flux conditions in the transmissibility calculations. Hence, an inactive edge will generally influence transmissibilities for the active edges in the region. This exact treatment of inactive edges is easily included in an implementation of the methods.

Due to the different couplings in the two methods, effects of an inactive edge in the interaction region will also differ. To demonstrate this, let the edge CE be inactive, as shown in Fig. 13. With AE as central edge, CE is unconstrained in the U-method, and the transmissibilities associated with edge AE is unaffected by CE being inactive for this method. Transmissibilities for the edges BE and DE are, however, influenced. With the O-method, all interaction-region transmissibilities are influenced by edge CE being inactive.

Now consider the case where edge DE is inactive, as shown in Fig. 14. Let $u_i = \overline{u}$; $i \neq 4$, and let $u_4 \neq \overline{u}$. Since the sum of the interaction-region transmissibilities equals zero, the flux across AE is then given by

$$f_A = t_{A4}(u_4 - \overline{u}) \tag{4.3}$$

for both the O- and the U-methods. Since CE is unconstrained in the U-method, and DE now is inactive, grid cell 4 does not enter the U-method flux molecule for edge AE. This is equivalent to t_{A4}, 0, and consequently, the flux f_A will be zero. For the O-method, grid cell 4 enters the flux molecule through its coupling to grid cell 3 at edge CE. Therefore, both t_{A4} and f_A will be nonzero.

These examples involving inactive edges tend to emphasize some underlying qualitative differences between the O- and U-methods.

4.4. *Numerical Examples*

Validation of the constructed methods for problems involving inhomogeneities and anisotropy is difficult, due to lack of available analytical solutions. However, results from various methods can be compared, and sometimes the ability to model certain known properties of the exact solution can be tested. Experience with the O- and the U-methods for both real and synthetic problems shows that differences in results are small. This section will present some model-problem examples with motivation and terminology from reservoir simulation.

For all examples, the total production rate will balance the total injection rate in the model, and simulation results will be presented for a time when a stationary solution is established. The homogeneous Neumann condition is applied at all boundaries. The letters I and P are used to indicate the location of injectors and producers, respectively. For comparison of solutions calculated by two methods A and B, the following value is defined for grid cell i:

$$d_i = \frac{u_i^{\mathrm{A}} - u_i^{\mathrm{B}}}{\Delta U}. \tag{4.4}$$

Here, ΔU is the difference between the largest and smallest grid-cell values in the solution variable. Differences between the various pairs of solutions have been measured with the 2-norm L_2, and the maximum norm L_∞, of the grid vector $\{d_i\}$.

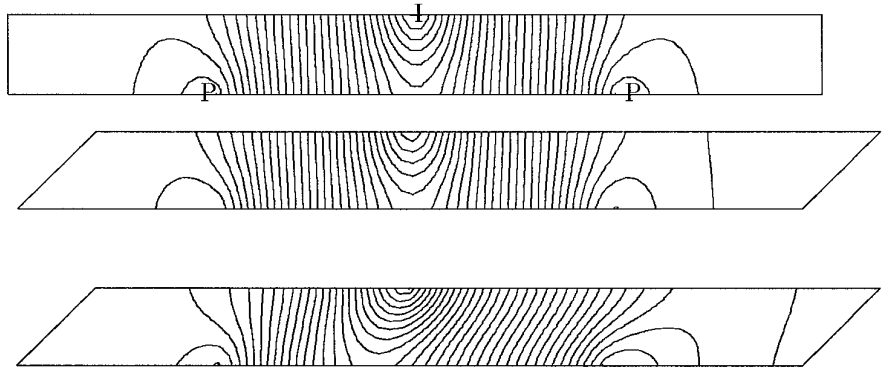

FIG. 15. Solution level curves for a three-well problem.

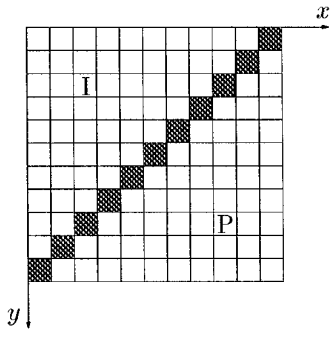

FIG. 16. Diagonal-shaped permeability contrast.

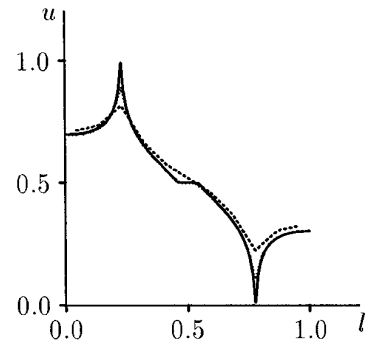

FIG. 18. O-method. High-permeable diagonal-shaped permeability contrast. $\theta = 135°$.

The first numerical example is based on a homogeneous and isotropic **K**, where the exact solution u is known to have a symmetry property: Two producing wells and a single injector are located symmetrically in a rectangular region, as shown in the upper part of Fig. 15. This part of the figure also shows level curves for the solution u, calculated with a Cartesian, orthogonal, and uniform grid and a standard two-point flux discretization. The grid dimension is 41×41. The rectangle boundaries are defined with a ratio 1:10, to minimize influence of the vertical boundaries on the solution profile.

The grid is then twisted 45° to produce a uniform, skewed grid. A similar model problem is often used to validate discretizations for multi-phase problems [10]. The center part of Fig. 15 shows the solution calculated with the O-method, and the lower part presents results from calculations with a two-point flux discretization [11]. The grid-line direction is clearly visible in the two-point flux-molecule solution. The O-method solution is not completely symmetric, but it is much closer to the solution on the orthogonal grid.

Comparing the O- and the U-methods, the value of d_i is less than 0.01 for all grid cells, except in the three cells perforated by wells, where d_i is approximately 0.04.

The above test example does not include inhomogeneities or anisotropy. The ability to handle inhomogeneities in combination with full-tensor anisotropy and/or grid non-orthogonality, is what the methods are designed for. The next test examples involve full-tensor anisotropy in combination with jump discontinuities in **K**. For simplicity, all grids will now be orthogonal and uniform. The main objective is to examine convergence of the methods when the grid is refined.

Two model problems have been used for this investigation, as shown with the 11×11 base grid in Fig. 16 and Fig. 17. A single producer and a single injector is located in the same grid diagonal, in the following, referred to as the *well-diagonal*. Within each region, white and shaded, the permeability is constant, and $\mathbf{K}(\text{shaded}) = \kappa\mathbf{K}(\text{white})$. Results will be presented for $\kappa = 100$ and $\kappa = 0.01$.

The permeability tensor incorporates a global anisotropy with an anisotropy ratio $k_{\text{small}}/k_{\text{large}}$ equal to 0.1, k_{small} and k_{large} being measured along the principal directions of **K**. The angle between the "small" principal axis and the x-axis, will be denoted θ. A maximum anisotropy effect is found for angles $\theta = 45°$ and $\theta = 135°$, with either the small or the large principal direction coinciding with the well-diagonal.

For both the O- and the U-methods, convergence has been investigated by using refined grids of dimension

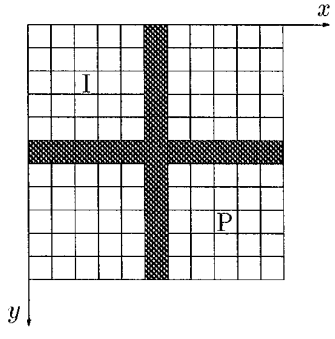

FIG. 17. Cross-shaped permeability contrast.

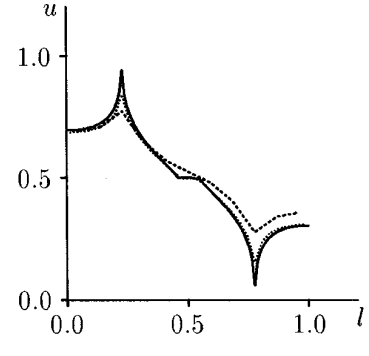

FIG. 19. U-method. High-permeable diagonal-shaped permeability contrast. $\theta = 135°$.

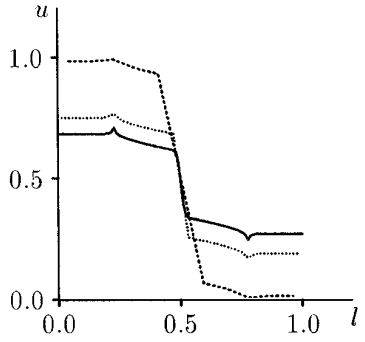

FIG. 20. O-method. Low-permeable diagonal-shaped permeability contrast. $\theta = 45°$.

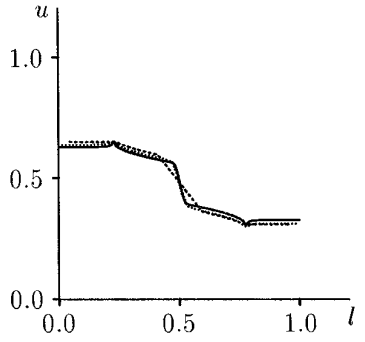

FIG. 21. U-method. Low-permeable diagonal-shaped permeability contrast. $\theta = 45°$.

33×33 and 99×99. Discontinuity configurations are fixed in space and unaffected by grid refinement. Based on the grid vector $\{d_i\}$, defined in (4.4), comparison between the O- and the U-methods has been performed for various values of the inhomogeneity factor κ and the anisotropy angle θ. For both models and almost all permeability distributions, excellent agreement is found for the finest grid, in both L_2 and L_∞, so that the arithmetic average can be regarded as a quasi-exact solution. For almost all cases, the O- and the U-methods are found to agree very well, even on the coarser grids. Also, convergence of the two methods towards the quasi-exact solution is found to be very similar, as the grids are refined.

Despite the similarity of the results from the two methods, some systematic properties are still indicated by the experiments: Generally, the O-method is found to resolve the solution close to a strong source/sink slightly better than the U-method, while the U-method approximates the solution close to certain discontinuities better than the O-method. This will be demonstrated by presenting results from two selected parameter sets with the diagonal-shaped permeability contrast:

Consider the variation in the solution variable u, sampled along the well-diagonal. Figure 18 and Fig. 19 show results produced by the O- and the U-methods, respectively, for a test problem with a high-permeable shaded region, $\kappa = 100$ and anisotropy angle $\theta = 135°$. Solid curves correspond to fine-grid solutions, dashed curves to coarse-grid solutions, and solutions on the 33×33-grid are shown by dotted curves. The plotted data have been scaled to lie within the unit square. The sharp maximum and minimum in the fine-grid solutions correspond to the locations of the wells. Differences between the methods are small, but the rapid variation in u in the vicinity of wells is resolved slightly better by the O-method than by the U-method on the coarse grid.

Results for a low-permeable shaded region, $\kappa = 0.01$ and with an anisotropy angle $\theta = 45°$ are shown in Fig. 20 and Fig. 21. Significant differences are found on the coarsest grid for this case. The variation caused by the staircase discontinuity is much better resolved by the U-method than by the O-method. Differences in the solutions on the coarser grids diminish as θ moves away from 45°, but they are significant for $\theta \in (20°, 70°)$. The large discrepancies between the O- and the U-methods seen in the latter example have not been found in any other of the cases investigated.

4.5. *Analysis of Special Flow Situations*

In most cases, solutions produced by the O- and the U-methods behave very similarly, and no general preference towards one of the methods has been found. Still, the examples presented in the previous section indicate two situations where the methods behave differently, and these will be investigated closer using the mechanistic description introduced in Section 3.5. For both methods, continuity conditions at the central edge are identical, so the differences will be explained by studying couplings at the remaining edges.

4.5.1. *Strong Point Singularity.* Test examples indicate that the O-method resolves the rapid variation around a well in a low-permeable medium slightly better than the U-method. In this situation, the well represents a strong point singularity in the model problem. Consider a point singularity located in grid cell 5 in Fig. 22, in a homogeneous, but anisotropic medium. (Note that the local num-

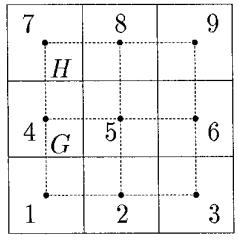

FIG. 22. Some grid cells with interaction regions.

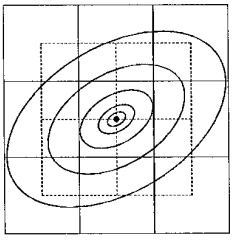

FIG. 23. Equipotential curves close to a point singularity in a homogeneous, anisotropic medium.

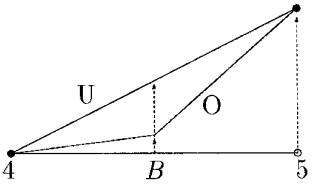

FIG. 25. O- and U-methods. Resolution of point singularity in homogeneous medium.

bering of grid cells and planes associated with an interaction region, used elsewhere in the paper, will not be applied here.)

Equipotential curves for the exact solution are sketched in Fig. 23. Assume for the numerical solution that $u_i \approx \bar{u}$; $i \neq 5$, and $u_5 \gg \bar{u}$.

Let H be a central edge in the U-method, defined inside the interaction region spanned by grid cells 7, 4, 5, and 8. Figure 24 illustrates the mechanistic behavior of the U-method for plane 4 and plane 5 in this interaction region.

Due to the medium homogeneity and the complete link between plane 4 and plane 5 along BE, these two planes will behave as a single plane in the U-method. For the O-method, the coupling along BE is weaker; confer Fig. 6. To illustrate the significance of this observation, consider the curve traced out in the planes when moving in a straight line from grid point 4 to grid point 5. In Fig. 25 such curves are sketched for both methods. The O-method is seen to resolve the rapid variation in the solution better than the U-method.

For the U-method, the flow pattern around the singularity also shows an unexpected behavior: Let G be a central edge in the interaction region formed by the four cells 4, 1, 2, and 5, and consider fluxes across the interface segments G and H:

$$f_G = \sum_i t_{Gi} u_i \approx t_{G5}(u_5 - \bar{u}),$$
$$f_H = \sum_j t_{Hj} u_j \approx t_{H5}(u_5 - \bar{u}). \tag{4.5}$$

The approximations follow from the assumption $u_i \approx \bar{u}$; $i \neq 5$. From the analytical flux expressions stated for the U-method in (4.2), it follows that $\operatorname{sgn} t_{G5} = \operatorname{sgn} t_{H5}$. Hence, $\operatorname{sgn} f_G = \operatorname{sgn} f_H$: If fluid flows into cell 4 through interface G, it then leaves the same cell through interface H, which is not in accordance with the expected flow pattern radiating from a strong point source. For the O-method, t_{G5} and t_{H5} may have equal or opposite signs, depending on the anisotropy ratio and angle.

4.5.2. *Large Jump Discontinuity.* In the numerical test examples, the U-method is found to resolve the solution in the vicinity of certain jump discontinuities better than the O-method. Figure 26 is a detail of the permeability distribution close to a discontinuity of this type, where the shaded area has a significantly lower permeability than the white area. Assume that no point singularity exists in the immediate vicinity of the discontinuity. Equipotential curves for the exact solution close to the discontinuity will be as indicated in Fig. 27. Consider the interaction region spanned by the grid cells 8, 5, 6, and 9, with central edge H. One of the non-central edges (bold line) coincides with a part of the discontinuity. For the U-method, this is the only part of the discontinuity influencing the transmissibility calculations for edge H, as the interface between grid cells 6 and 9 is unconstrained. From the mechanistic description it is seen that a discontinuity coinciding with a non-central edge is treated very accurately by the U-method.

Similar situations arise when considering other edges in the vicinity of the discontinuity. Non-central edges frequently coincide with the discontinuity, as two out of the three constrained edges involved in the transmissibility calculations in the U-method are non-central. This explains why the U-method resolves the discontinuity better than

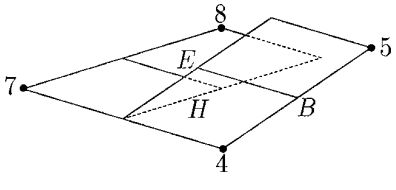

FIG. 24. U-method. Mechanistic behavior for homogeneous medium.

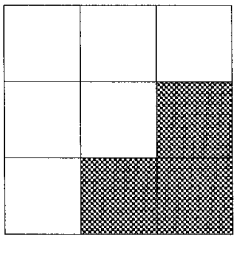

FIG. 26. Permeability map.

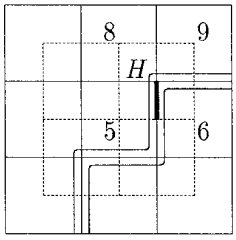

FIG. 27. Equipotential curves close to a large jump discontinuity.

the O-method and supports numerical results from Section 4.4.

Even this motivation does not fully explain why differences are significantly larger for the example in Figs. 4.10 and 4.11 than for other data sets. The complete explanation is somewhat lengthy [2], and must be left out due to space limitations. However, four combined conditions seem to be necessary to provoke such large differences [2]:

(1) A ''staircase'' distribution of the low permeable region.

(2) A large jump discontinuity.

(3) A relatively small anisotropy ratio, $k_{\text{small}}/k_{\text{large}}$.

(4) An anisotropy angle θ closer to 45° than to 0°.

4.6. *Hybrid Methods*

Although none of the two methods shows general superiority, different potential distributions have been shown to favor each of the methods. Regions in space where such potential distributions are likely to occur are often known a priori. It may then be worthwhile to construct hybrid methods, where the O- and U-methods are applied in their respective favorable regions.

5. CONCLUSIONS

The main conclusions of this paper are:

• Two classes of discretization methods for quadrilateral grids have been presented and analyzed.

• Both O- and U-methods are able to handle media inhomogeneity, in combination with full-tensor anisotropy and/or grid non-orthogonality.

• Numerical results obtained with the methods for curvilinear grids agree very well, in general. Second-order accuracy has been shown for a class of problems, including a uniform grid on a homogeneous medium.

• Significant and/or systematic differences between the methods are found only for special potential distributions. Regions in space where such potential distributions are likely to occur are often known a priori, and hybrid methods may then be advantageous.

ACKNOWLEDGMENTS

We thank the management of Norsk Hydro for allowing us to publish this paper. The paper is part of Norsk Hydro's contribution to the Commission of the European Union's *Joule program*, subprogram *Energy from Fossil Sources, Hydrocarbons,* founded in part by the Research Council of Norway.

REFERENCES

1. I. Aavatsmark, T. Barkve, Ø. Bøe, and T. Mannseth, ''Discretization on Non-orthogonal, Curvilinear Grids for Multi-phase Flow,'' in *Proceedings, 4th European Conference on the Mathematics of Oil Recovery, Røros 1994.* (unpublished).
2. I. Aavatsmark, T. Barkve, Ø. Bøe, and T. Mannseth, unpublished.
3. K. Aziz and A. Settari, *Petroleum Reservoir Simulation* (Appl. Sci., London, 1979.)
4. G. Chavent and J. Jaffré, *Mathematical Models and Finite Elements for Reservoir Simulation* (North Holland, New York, 1986).
5. P. I. Crumpton, G. J. Shaw, and A. F. Ware, *J. Comput. Phys.* **116,** 343 (1995).
6. L. J. Durlofsky, *J. Comput. Phys.* **105,** 252 (1993).
7. M. G. Edwards and C. F. Rogers, ''Multigrid and Renormalization for Reservoir Simulation,'' in *Proceedings, 4th European Multigrid Conference, Amsterdam 1993,* edited by P. W. Hemker and P. Wesseling (Birkhäuser, Basel, 1994.) p. 189.
8. M. G. Edwards and C. F. Rogers, ''A Flux Continuous Scheme for the Full Tensor Pressure Equation,'' in *Proceedings 4th European Conference on the Mathematics of Oil Recovery, Røros, 1994* (unpublished).
9. I. Faille, ''Control Volume Method to Model Fluid Flow on 2D Irregular Meshing,'' in *Proceedings, 2nd European Conference on the Mathematics of Oil Recovery, Arles, 1990,* edited by D. Guérillot and O. Guillon (Éditions Technip, Paris, 1990), p. 149.
10. T. M. Hegre, V. Dalen, and A. Henriquez, ''Generalized Transmissibilities for Distorted Grids in Reservoir Simulation,'' Paper SPE 15622, in *Proceedings, SPE 61st Annual Technical Conference and Exhibition, New Orleans, 1986.*
11. D. K. Ponting, ''Corner Point Geometry in Reservoir Simulation,'' in *Proceedings, 1st European Conference on the Mathematics of Oil Recovery, Cambridge, 1989,* edited by P. R. King (Clarendon Press, Oxford, 1992), p. 45.
12. B. J. Rozon, ''A Generalized Finite Volume Discretization Method for Reservoir Simulation,'' Paper SPE 18414, in *Proceedings, SPE 10th Symposium on Reservoir Simulation, Houston, 1989,* p. 71.
13. G. E. Schneider and M. J. Raw, *Numer. Heat Transfer* **9,** 1 (1986).
14. J. F. Thompson, Z. U. A. Warsi, and C. W. Mastin, *Numerical Grid Generation: Foundations and Applications* (North Holland, New York 1985.)
15. J. L. Yanosik and T. A. McCracken, *Soc. Pet. Engr. J.* 253 (1979).